Made available through Montana State University's [ScholarWorks]

Simple near-monostatic Mueller polarimeter

Nathaniel J. Field, Joseph A. Shaw

© 2024 Optical Society of America. One print or electronic copy may be made for personal use only. Systematic reproduction and distribution, duplication of any material in this paper for a fee or for commercial purposes, or modifications of the content of this paper are prohibited.

Accessibility Disclaimer:

For a more accessible version of this document, please submit an accessibility request form through the Montana State University Library website.

Simple near-monostatic Mueller polarimeter

NATHANIEL J. FIELD[1] AND JOSEPH A. SHAW[1,2,*]

[1] Electrical & Computer Engineering Dept., Montana State University, Bozeman, MT USA 59717
[2] Optical Technology Center, 334 NAH, Montana State University, Bozeman, MT USA 59717
[*] joseph.shaw@montana.edu

Compiled September 4, 2024

Inferring material properties from active or passive polarimetric remote sensing requires knowledge of the polarized bidirectional reflectance distribution function (P-BRDF). To encourage and simplify the process of measuring the P-BRDF of materials in the monostatic or near-monostatic configurations seen in lidar and other active remote sensing systems, we describe the design, build, and operating procedure for a simple near-monostatic polarimeter. The described system operates at 1064 nm and with a transmitter-receiver separation of about 4°, but the design principles, alignment procedure, and measurement procedure can be directly applied to systems at other wavelengths or separation angles. Also included are the control and data analysis software for the instrument we deployed, and a small selection of retrievals from the instrument.

http://dx.doi.org/10.1364/ao.XX.XXXXXX

---

1. INTRODUCTION

Polarization represents a significant means of improving data density in combination with the more common retrieved light characteristics: intensity, spatial frequency, and spectral distributions. To date, polarization-enhanced remote sensing has focused primarily on passive methods [1] and dual-polarization lidar [2].

Polarization-enhanced lidar has been used for a wide variety of applications, especially in atmospheric and oceanic remote sensing [2]. It has also been used to improve the detection of submerged samples with sensors above the water [3]. Foliage and plant species discrimination are areas of interest in active polarimetric sample discrimination, including imaging polarimeters [4, 5], active lab-based polarimetry [6], and dual-polarization lidars [7]. There is also opportunity to improve material discrimination in complex scenes using polarimetry, as demonstrated in previous passive systems [8] and active systems [9, 10].

To more accurately identify samples in a scene, the community requires means to characterize reference materials specific to their applications, similar to those which exist for satellite or other passive remote sensing systems. Data from previous works report material polarimetric responses by their polarized bidirectional reflectance distribution function (P-BRDF) [6, 11–14]. However, of these reported P-BRDFs, only those in [13] included measurements of the monostatic configuration, the most common configuration for lidar and similar active polarimetry. These monostatic P-BRDF (P-mBRDF) returns are important for polarization-enhanced lidar with applications moving toward material discrimination.

In this paper, we describe the design, operating procedure, and data analysis methods for a simple near-monostatic polarimeter. We also show some data collected by the instrument we built, the LabView collection software we developed, and the MATLAB data analysis script used to process the raw intensity data into Mueller matrix P-mBRDF plots.

2. BACKGROUND

For material discrimination, we are primarily interested in determining Mueller matrix, $\mathbf{M}$, values, which represent material properties. In active polarimetry, we use a polarization state generator (PSG) in combination with a light source, such as a laser, to illuminate the scene with known polarization characteristics, $\mathbf{S_G}$. Optical detectors are only directly capable of detecting the power or photon flux incident on their active surface, so a polarization state analyzer (PSA) with a known polarization response, $\mathbf{M_A}$, is used to attenuate total power as a function of the incident light's polarization state. Extended to an equation, the PSG-PSA active polarimetric system is described as

$$\mathbf{S_{det}} = \begin{bmatrix} S_{0,det} \\ S_{1,det} \\ S_{2,det} \\ S_{3,det} \end{bmatrix} = \begin{bmatrix} I_{det} \\ Q_{det} \\ U_{det} \\ V_{det} \end{bmatrix} = \mathbf{M_A} \mathbf{S_{Rx}} = \mathbf{M_A} (\mathbf{M_{samp}} \mathbf{S_G}), \quad \textbf{(1)}$$

where $\mathbf{S_{det}}$ describes the light at the detector and $\mathbf{M_{samp}}$ describes the polarization sensitive properties of the sample in the scene. As seen above, a Stokes vector can be broken down into its four components. The S_0 or I element represents the total power regardless of polarization, and is the only element measured by the detector's active area. As such, we require a minimum of 16 unique measurements to fully reconstruct an unknown $\mathbf{M_{samp}}$. This is most often accomplished by setting four PSG states and four PSA states and performing measurements for each of the unique PSG-PSA state combinations.

Optimization of polarimetry systems primarily concerns proper selection of these PSG and PSA states. As shown in previous literature, optimal PSG states are those matched to the

PSA states [15, 16]. Selecting optimal PSA states is best conceptualized using the Poincaré sphere, where optimal polarization states have Poincaré coordinates which define a regular polyhedron [17, 18]; for four PSA states, this generates a regular tetrahedron.

Following the processes in previous literature, we can quantify the maximum error propagation for transmitter and receiver errors, including noise, by determining the condition number, κ, of the PSG and PSA system matrices [16, 18]. The condition number for the PSG, κ_G, represents the maximum error propagation of intensity or polarization noise in the Tx source. The condition number for the PSA, κ_A, represents the maximum error propagation of noise in the Rx detector.

To find κ for each branch of the radiometer, we use

$$\kappa(\mathbf{A}) = ||\mathbf{A}||_2 \, ||\mathbf{A}^{-1}||_2 = \frac{\sigma_{max}(\mathbf{A})}{\sigma_{min}(\mathbf{A})}, \tag{2}$$

where $|| \cdot ||_2$ is the L^2 norm, σ_{max} and σ_{min} are the maximum and minimum singular value decompositions, and $\mathbf{A}$ is the analysis matrix of the system's polarization elements, defined as

$$\mathbf{A} = \begin{bmatrix} \mathbf{M_0^1} \\ \mathbf{M_0^2} \\ \mathbf{M_0^3} \\ \mathbf{M_0^4} \end{bmatrix} = \begin{bmatrix} m_{00}^1 & m_{01}^1 & m_{02}^1 & m_{03}^1 \\ m_{00}^2 & m_{01}^2 & m_{02}^2 & m_{03}^2 \\ m_{00}^3 & m_{01}^3 & m_{02}^3 & m_{03}^3 \\ m_{00}^4 & m_{01}^4 & m_{02}^4 & m_{03}^4 \end{bmatrix}, \tag{3}$$

where $\mathbf{M_0^i}$ is the first row of the combined Mueller matrix of the polarization elements for the PSG's or PSA's ith state. When A is singular (or near-singular) you may need to use the pseudo-inverse of A in Eq. 2 instead of the simple A^{-1} inverse. For an optimal configuration, the condition number of the PSG and PSA are each equal to $\sqrt{M-1}$, where M is the dimensionality of the polarization (3 for linear systems and 4 for full-polarimetric systems). Therefore, an optimal system will have $\kappa_G = \kappa_A = \sqrt{2}$ for a linear polarimetry system, or $= \sqrt{3}$ for a full-polarimetric system.

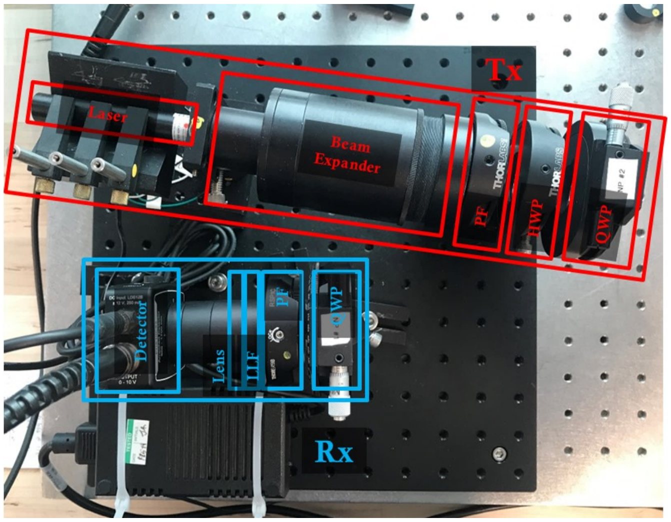

Fig. 1. Overhead image of the simple polarimeter, with the transmitter optics labelled in red and the receiver optics labelled in blue. This figure is a partial reproduction of a figure in [19].

3. INSTRUMENT DESIGN

A. Example Design

In this section, we walk through the design of the active polarimeter we built, and provide reasoning such that others could design similar systems at different wavelengths using the same principles. An overhead view of the system we built is shown in Fig. 1 with components labelled.

The instrument begins with a simple active radiometer: a laser transmitter (Tx) and a photodiode receiver (Rx). The system we built used a 10-mW, 1064-nm, diode-pumped solid-state laser and a ThorLabs PDA10CS2 photodiode, which is an InGaAs, variable-gain detector with a 1-mm-diameter circular active area. To reduce speckle effects, the 1-mm-diameter laser beam was expanded by a 10x beam expander; this also increased the beam divergence from about 0.5 mrad to 5 mrad. For the receiver optics, we used a single 50-mm-focal-length plano-convex lens with a 25-mm clear aperture, resulting in a full field-of-view (FOV), ω_{FOV}, of 10 mrad, which is about double the transmitter beam divergence. Placing the planar side toward the detector and the convex side toward the scene minimizes aberrations for the simple lens system. Finally, a 10-nm bandwidth laser-line spectral filter (LLF) for a 1064-nm central wavelength was placed on the scene side of the receiving optics to eliminate the majority of background light from the scene.

The PSG was inserted in front of the transmitter and consisted of a linear polarizing filter (PF), a half-wave retarder (HWP), and a quarter-wave retarder (QWP). The PF was locked to transmit vertical linear polarization, and the laser was rotated in its mount until maximum transmittance through the filter was achieved. This provided a much purer initial polarization state than the laser alone, since the PF used has an extinction ratio of approximately 10^3. The HWP was set in a rotation mount, which allowed us to rotate the initial linear state to other orientation angles without attenuation. The QWP was set with its fast axis at 45° on a 90° flip-mount, allowing it to be inserted into or removed from the optical path quickly and easily.

The PSA was inserted in front of the receiver optics and consisted only of a QWP and a PF. The QWP was set to -45° on a 90° flip-mount for the same purpose as in the PSG. The PF was set in a rotation mount to allow for preferential attenuation for different linear orientation angles.

For an analog-digital converter (ADC), we used a National Instruments USB-6001 data acquisition device. For a total list of parts, excluding some minor optomechanical mounting equipment, see Table 1.

B. System Analysis

For the purposes of compiling and potentially sharing reference measurements, it's important to know the specifications of the systems acquiring the reference data. Some critical system information includes the operating wavelength, actual geometric separation angle between transmitter and receiver, receiver FOV, and other specifications for which we give an example summary in Table 2.

The operating wavelength is critical information as many materials exhibit reflectance and transmittance characteristics which are strongly spectrally dependent. To a lesser extent, the receiver optical bandwidth can also be useful information when considering the spectral effects on the sample characteristics. The transmitter beam diameter at the output, beam divergence, and beam diameter at the sample help inform the probability of speckle error and the total illumination area considered for

Table 1. Developed System Parts and Approximate Costs

Part	Cost, $
Laser (Edmund Optics #37-043)	350
Detector (ThorLabs PDA10CS2)	475
PF (Meadowlark DPM-100-NIR2-1) ×2	2 × 685
HWP (Meadowlark NHM-100-1064)	575
QWP (Meadowlark NQM-100-1064) ×2	2 × 575
ADC (NI USB-6001)	300
Rotation Mount (ThorLabs RSP1) × 5	5 × 100
Flip Mount (ThorLabs FM90) × 2	2 × 100
Lenses	100
total	5,020

samples with spatial anisotropy. The viewing solid angle, Ω_v, which should be relatively narrow for the purpose of P-mBRDF characterization, is determined by the smaller of the solid angles produced by Eq. 4 or Eq. 5.

$$\Omega_v^{FOV} = 4\pi \sin^2(\frac{\omega_{FOV}}{4}) \tag{4}$$

$$\Omega_v^{A} = \frac{A_s}{Z^2} = \frac{\pi D_s^2}{4Z^2} \tag{5}$$

Finally, the actual geometric separation angle between the transmitter and receiver is critical to report the actual monostatic or near-monostatic nature of the characterizing measurement.

The signal-noise ratio (SNR) for the developed system was calculated using a theoretical signal for a 10% Lambertian reflector against the detector noise equivalent power (NEP). In a lab setting, the optical power incident on the detector, P_{Rx}, follows a basic radiometric equation,

$$P_{Rx} = A_{Rx}\Omega_v L_s = \frac{\pi D_{Rx}^2}{4}\Omega_v \frac{4 I_{Tx}\rho_s T_{atm}}{\pi^2 D_s^2} = \frac{D_{Rx}^2 \Omega_v I_{Tx}\rho_s T_{atm}^2}{\pi D_s^2}, \tag{6}$$

where ρ_s is the reflectance of a Lambertian sample reflector and T_{atm} is the transmittance of the atmosphere (typically about 1 in a lab setting). For the developed system, P_{Rx} comes out to about 0.269 μW, and the maximum NEP for the detector is 0.166 μW, giving an initial SNR of 1.62, or equivalently, 4.2 dB. The ADC has a sampling rate of 20 kS/s, so averaging over 0.5 seconds gives 10,000 samples, and improves the SNR by a factor of 100, to about 162, or equivalently, 44.2 dB.

For ease of use, the nearest-optimum states we can select are a circular state (RHC) and three linear states with orientations equally separated by 60°, which we select as 0°, 60°, and 120°. Using these states for both PSG and PSA, the condition numbers are $\kappa_G = \kappa_A \approx 2.48$. This means any output intensity noise after the clean-up polarizer, whether due to intensity or polarization instability in the laser, can propagate to the polarization measurements with a maximum magnification of 2.48. Similarly, noise in the detector can propagate to Mueller matrix element calculation with a maximum magnification of 2.48. These κ values are only about 43% greater than those for the optimal Mueller polarimeter, $\sqrt{3} \approx 1.73$.

The maximum error propagation reduces the SNR of the polarimetric results as compared to the system SNR.

$$SNR_{pol} = \frac{SNR_{sys}}{\kappa_A} \tag{7}$$

The values are summarized in Table 2.

Table 2. Developed System Specifications

Parameter	Value
Operating wavelength, λ	1064 nm
Receiver optical bandwidth, $\Delta\lambda$	±5 nm
Transmitter optical power, I_{Tx}	10 mW
Beam diameter at output, D_b	10 mm
Beam divergence, ω_{div}	5 mrad
Beam diameter at sample, D_s	13.8 mm
Distance to sample, Z	762 mm
Receiver aperture diameter, D_{Rx}	25 mm
Full FOV, ω_{FOV}	10 mrad
Tx-Rx separation angle, θ_Δ	4°
Sample rotation axis	y-axis (vertical)
System signal-noise ratio, SNR_{sys}	162 (44.2 dB)
Max error propagation, $\kappa_G = \kappa_A$	2.48
Min polarimetric SNR, SNR_{pol}	65.3 (36.3 dB)

4. OPERATING PROCEDURE AND DATA ANALYSIS

A. Optomechanical Alignment

Alignment of the polarimeter optical trains is relatively straightforward. Use multiple irises to align a beam expander or similar optics along the transmitter optical path. For the receiver, a lens tube attached to the detector containing the focusing lens at its focal length from the detector active area is typically sufficient for axial alignment. Measuring the focal length separation to within about 1% error is generally sufficient for this type of radiometry as it is non-imaging.

After inserting an LLF, or while in a dark lab, but before inserting the polarization elements, use a diffuse reflectance sample and rotate either the transmitter or receiver optical paths until you receive a maximum signal. Lock the transmitter and receiver in place and note the geometric separation angle, θ_Δ, of their optical paths. Also, note the maximum signal you achieved; this will help in polarizer alignment.

The angular geometry used in the data we gathered is summarized in Fig. 2, which is useful for similar fixed-separation systems. The reference 0° angle is where the sample surface normal is pointed halfway between the optical axes of the transmitter and receiver. Rotations of the surface normal toward the transmitter are referred to with positive angles, and rotations toward the receiver are referred to with negative angles.

Next, insert the transmitter PF with its transmission axis as horizontal as possible; most rotation mounts should allow for 1° (17.5 mrad) tolerance or better on this orientation angle. For the purposes of this procedure, horizontal orientation is 0°, vertical

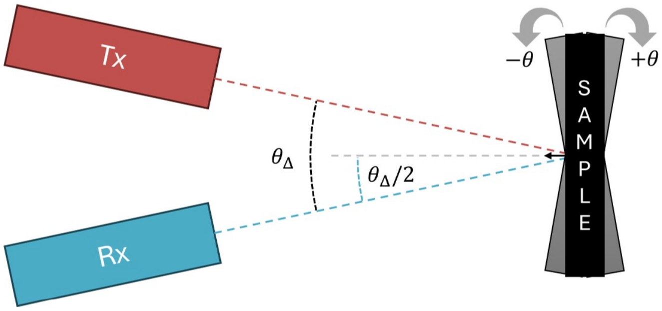

Fig. 2. Overhead diagram depicting the geometric separation angle, the surface-normal 0° reference setup, and the general orientation of positive and negative viewing/illumination angles.

orientation is 90°, and 45° orientation is above horizontal and to the right of vertical when looking into the beam. If possible, rotate the laser head to maximize the power through the polarizer, as measured by the aligned receiver. Otherwise, you might consider rotating the PF to achieve max power throughput, shifting the suggested orientation angles of each of the other polarizer elements by the same amount. Lock the transmitter PF in place.

Then insert the receiver PF and rotate it until you have a minimum signal at the detector. Note the rotation angle as 90°, or otherwise at 90° from the transmitter PF orientation.

Leaving the receiver PF at this crossed orientation, insert the transmitter HWP and rotate it until you return to a minimum signal at the detector. Note this HWP orientation as the crystal axis aligned to the transmitter PF orientation (0° by default).

The transmitter QWP should be labelled with a fast-axis (sometimes referred to as the crystal axis). Insert the transmitter QWP and rotate it so that the fast axis is at about -45° from the transmitter PF orientation. Alternate the receiver PF between 0° and 90° (co- and cross-polarized with the transmitter PF) while rotating the QWP in small increments about -45° until the co- and cross-polarized signals are equal. This produces right-hand circular (RHC) polarization. Lock the transmitter QWP in place, then flip it out of the optical path and repeat this process with the receiver QWP but at and about +45° orientation.

B. Control & Analysis Software

The control software is programmed in LabView 2019. The software relies on drivers for the Newport USB-6001, but otherwise functions using basic LabView controls. This software is available in Code 1 (Ref. [20]).

The analysis software is programmed in MATLAB 2023a. This software loads .csv files as saved by the control software, reports the Mueller matrices as figures, and records the Mueller matrices as a function of angle in new .csv files, with each row of the file in the form $[\theta_v\ m_{00}\ m_{01}\ m_{02}\ m_{03}\ m_{10}\ \ldots\ m_{32}\ m_{33}]$. This software is available in Code 2 (Ref. [21]).

C. Data Collection Procedure

To characterize the P-mBRDF (or a fixed Tx-Rx separation P-BRDF) of a sample, either the sample or polarimeter must be rotated with respect to the other. In many cases, a fixed polarimeter with a rotating sample provides the most simply realized setup. We mounted samples on a stage rotating about the y-axis (vertical axis). The samples were set at about 0.75 m from the front of the transmitter and receiver (see Table 2 for specific values).

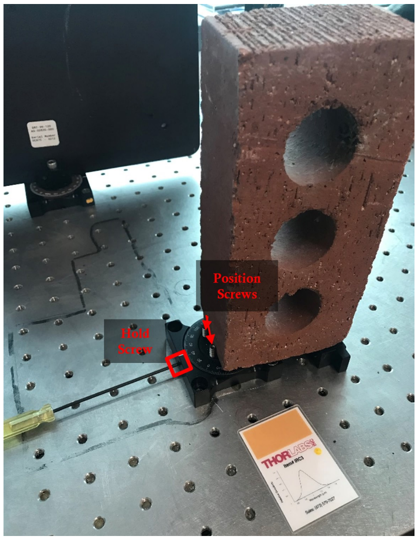

Fig. 3. Image of a red clay brick sample on a horizontal rotation stage. Two set screws make it easy to return the brick to the same position repeatably, and to more accurately determine the invidence/viewing angle, θ_v, relative to the polarimeter. This figure is a partial reproduction of a figure in [19].

When necessary, samples are prepared so they are planar. For example, a Spectralon reference or brick are rigid materials with a tall, flat face which does not need to be prepared. However, a roofing shingle or plant leaf are not rigid, and so must be attached to a backing surface such as a piece of wood in preparation. Once on a rigid surface of sufficient height, a horizontal rotation stage can be used as shown in Fig. 3 to make repeatable sample rotation much easier.

Once the sample is prepared and in place, follow the semi-time-optimized procedure here in combination with the control software noted above:

1. Set the sample at a known incidence angle.
2. Set the HWP_G to 0° and the PF_A to 0°. Flip the QWP_G and QWP_A out of the optical path.
3. In the control software, SCAN for Stage 1.
4. Flip the QWP_A into the beam path. SCAN for Stage 2.
5. Flip the QWP_G into the beam path. SCAN for Stage 3.
6. Flip the QWP_A out of the beam path. SCAN for Stage 4.
7. Rotate the PF_A to 60°. SCAN for Stage 5.
8. Flip the QWP_G out of the beam path. SCAN for Stage 6.
9. Rotate the PF_A to -60°. SCAN for Stage 7.
10. Flip the QWP_G into the beam path. SCAN for Stage 8.
11. Flip the QWP_G out of the beam path, rotate the HWP_G to -30°. SCAN for Stage 9.
12. Rotate the PF_A to 60°. SCAN for Stage 10.
13. Rotate the PF_A to 0°. SCAN for Stage 11.
14. Flip the QWP_A into the optical path. SCAN for Stage 12.
15. Rotate the HWP_G to 30°. SCAN for Stage 13.

16. Flip the QWP$_A$ out of the optical path. SCAN for Stage 14.
17. Rotate the PF$_A$ to 60°. SCAN for Stage 15.
18. Rotate the PF$_A$ to -60°. SCAN for Stage 16.
19. Set the sample to a new known incidence angle and repeat steps 2-19 until you have completed your angular analysis.

In this procedure, the polarizing elements are distinguished as being part of the PSA or PSG with a subscript A or G, respectively. For example, QWP$_A$ is the QWP in the PSA (receiver) arm of the polarimeter.

For our data collection efforts, we typically scanned from -60° to 60 °, or a smaller range on one side or the other for geometries where symmetry is expected or previously demonstrated. These angular limitations are primarily due to the illumination area overfilling some of the smaller samples as their projected area decreases.

Using this procedure, we have found that an experienced operator can complete a 16-measurement set in about 1 to 3 minutes, and a new operator can typically complete a measurement set in about 6-8 minutes. The total measurement time for a sample then depends on how many viewing/illumination angles are considered.

D. Data Structure and Analysis

The control software records measurement data as .csv files containing $N \times 17$ matrices, where N is the number of angles for which measurement sets were recorded. Each row is a 17-element matrix, with the first element giving the incidence-viewing angle, θ_v, and the remaining 16 elements giving the recorded signal (in mV) for each of the unique PSG-PSA states. The states are given in the order of vertical-vertical, vertical-60°, vertical-120°, vertical-circular, 60°-vertical, ... circular-120°, and circular-circular. This is the structure expected by the analysis software.

The data analysis is performed using linear regression to reduce processing time. The fundamental principle follows from a simple Mueller calculus equation,

$$\vec{S_{g,a}} = \begin{bmatrix} I_{g,a} \\ Q_{g,a} \\ U_{g,a} \\ V_{g,a} \end{bmatrix} = \mathbf{M_a} \mathbf{M_{samp}} \vec{S_g}, \tag{8}$$

where $\vec{S_{g,a}}$ is the Stokes vector of light reaching the detector, $\mathbf{M_a}$ is the analysis Mueller matrix, $\mathbf{M_{samp}}$ is the unknown Mueller matrix response of the sample, and $\vec{S_g}$ is the Stokes vector of the light generated in the transmitter arm. Since the detector can only measure intensity, the equation extends out to

$$\begin{aligned} I_{g,a} = {} & I_g(m_{a00}m_{s00} + m_{a01}m_{s10} + m_{a02}m_{s20} + m_{a03}m_{s30}) \\ & + Q_g(m_{a00}m_{s01} + m_{a01}m_{s11} + m_{a02}m_{s21} + m_{a03}m_{s31}) \\ & + U_g(m_{a00}m_{s02} + m_{a01}m_{s12} + m_{a02}m_{s22} + m_{a03}m_{s32}) \\ & + V_g(m_{a00}m_{s03} + m_{a01}m_{s13} + m_{a02}m_{s23} + m_{a03}m_{s33}), \end{aligned} \tag{9}$$

a simple linear combination equivalently represented as

$$I_{g,a} = \vec{B_{g,a}} \vec{A}, \tag{10}$$

where

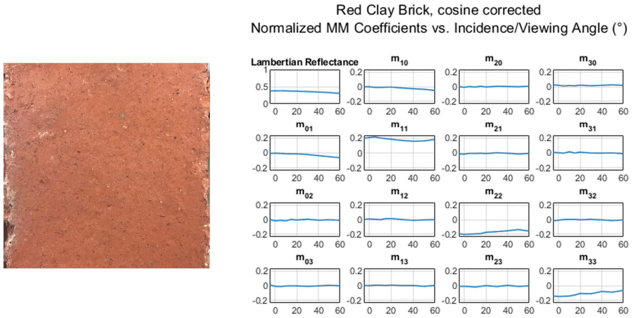

Fig. 4. An image of the sample brick surface about the measurement location (left) and the resulting P-mBRDF measurement (right).

$$\begin{aligned} \vec{A} = vec(\mathbf{M_{samp}}) = [& m_{s00}\ m_{s10}\ m_{s20}\ m_{s30}\ m_{s01}\ m_{s11}\ m_{s21}\ m_{s31} \\ & m_{s02}\ m_{s12}\ m_{s22}\ m_{s32}\ m_{s03}\ m_{s13}\ m_{s23}\ m_{s33}]^T \end{aligned} \tag{11}$$

and

$$\begin{aligned} \vec{B_{g,a}} = [& I_g m_{a00}\ I_g m_{a01}\ I_g m_{a02}\ I_g m_{a03} \\ & Q_g m_{a00}\ Q_g m_{a01}\ Q_g m_{a02}\ Q_g m_{a03} \\ & U_g m_{a00}\ U_g m_{a01}\ U_g m_{a02}\ U_g m_{a03} \\ & V_g m_{a00}\ V_g m_{a01}\ V_g m_{a02}\ V_g m_{a03}]. \end{aligned} \tag{12}$$

Extending Eq. 10 to the 16 measurements for each unique combination of g and a, we can expand the scalar $I_{g,a}$ to the 1x16 vector $\vec{I_{meas}}$, and expand the 1x16 vector $\vec{B_{g,a}}$ to the 16x16 matrix $\mathbf{B}$. Then, solving for $\vec{A}$, which is a simple vectorization of the sample Mueller matrix, we find

$$\vec{A} = \mathbf{B^{-1}} \vec{I_{meas}}. \tag{13}$$

5. EXAMPLE MATERIAL MEASUREMENTS

Some example data recorded with the example system design are presented here. These data represent the near-monostatic response of a red clay brick sample and a tar-fiberglass shingle sample, as previously reported in [19]. These data also have their m_{00} elements normalized to the near-normal returns of a Spectralon Lambertian reference of known reflectance. The plots shown here are also available in greater resolution in [19].

The red clay brick sample, shown in Fig. 4, was relatively matte and of middling reflectance at the operating wavelength. As such, we expect relatively flat reflectance across θ_v, with a slight dip at steeper angles and a moderate increase in polarizance and diattenuation at steep angles as well. These features can be observed in the results shown in Fig. 4, and we can also see that the off-diagonal elements for rotation and phase offset are minimal relative to the diagonal elements.

A tar-fiberglass shingle was also measured, as seen in Fig. 5. This sample was the least in-line with expected Lambertian or specular surface responses. The shingle consisted primarily of 1- to 3-mm diameter rough fragments of tar overlaying a thin layer of fiberglass insulation which was still visible in places through the tar. The reflectance was fairly Lambertian, at least in line with the brick's. Likely due to the high anisotropy of the tar

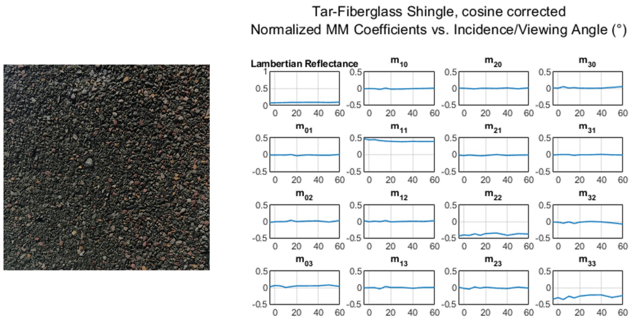

Fig. 5. An image of the sample tar-fiberglass shingle surface about the measurement location (left) and the resulting P-mBRDF measurement (right).

fragments, there was also no significant increase in polarizance and diattenuation at steeper θ_v. For a rough surface, we would expect a reduction in polarization maintenance (the diagonal elements), but we see relatively strong maintenance in this sample. Dark surfaces and specular reflectors both have stronger polarization maintenance, and it is unclear for such a complex sample if this effect is due to the darkness of the tar or the high reflectance of the visible regions of fiberglass.

6. DISCUSSION

We have discussed the purpose, theory, and design principles for simple monostatic and near-monostatic polarimeters. The example design and cited software serve to enable groups with shared interest in active polarimetry for sample discrimination to develop their own reference measurements.

One of the major limitations of our example system is that it records only at 1064-nm wavelength. As spectral characteristics of materials change, their polarimetric responses are all but certain to change as well. For groups aiming to make a simple instrument to characterize materials for other devices at specific operating wavelengths, such as a lidar operating at a single wavelength, this narrow spectral reference will work well so long as the simple polarimeter has the same wavelength as the main device.

The other limitation of our example system is that it is not truly monostatic. The system for which we were generating sample references was not truly monostatic, so a near monostatic was sufficient for our research. If, however, a true monostatic geometry is preferred, a group could use a non-polarizing beamsplitter in front of the Tx output which reflects some of the Tx signal into a beam-block, then reflects a fraction of the return signal out of the primary optical path to a Rx setup on the reflected path. This option produces a true-monostatic geometry, but may complicate design due to higher power requirements to produce similar SNR.

Another consideration, given the longer time scale of the measurement sets, is the transmitter power stability, and by extension, its polarization stability. This is relatively simply measured by placing the transmitter source behind the clean-up polarizer and firing into a detector, taking constant measurements for about 15 to 20 minutes. The laser need only be stable (not changing significantly) over the time period typical of a 16-measurement set; about 1-3 minutes for an experienced operator or 6-8 minutes for a newer operator.

Though it results in a much more expensive system, motorized rotation stages can be used in place of the manual rotation stages. In such a system, it is similarly efficient to realize a polarimetrically optimized set of PSG-PSA state combinations. For such a setup, we recommend the following four states for the unique states of the PSG and PSA individually, reported as their Poincarè coordinates $(2\theta_P F, \phi_\Delta, DoP)$: (0°, 90°, 1), (0°, -19.4712°, 1), (120°, -19.4712°, 1), and (-120°, -19.4712°, 1).

Funding. This project was funded by the Air Force Research Lab via a subcontract from S2 Corp through award FA8650-16-C-1954 with a fundamental research exception.

Disclosures. The authors declare no conflicts of interest.

Data Availability Statement. Data underlying the results presented in this paper are available to view in Ref. [19]. Additional data underlying the results presented in this paper are not publicly available at this time due to continuing efforts to create a publicly accessible database of P-mBRDF references, but our data may be obtained from the authors upon reasonable request.

REFERENCES

1. J. S. Tyo, D. L. Goldstein, D. B. Chenault, and J. A. Shaw, Appl. Opt. **45**, 5453 (2006).
2. K. Sassen, Proc. SPIE **5158**, 151 (2003).
3. M. Floc'h, G. L. Brun, C. Kieleck, *et al.*, Pure Appl. Opt. J. Eur. Opt. Soc. Part A **7**, 1327 (1998).
4. V. C. Vanderbilt, L. Grant, and C. S. Daughtry, Proc. IEEE **73**, 1012 (1985).
5. C. Rodríguez, E. Garcia-Caurel, T. Garnatje, *et al.*, Sci. reports **12**, 14743 (2022).
6. D. H. Goldstein and J. L. Cox, Proc. SPIE **5432**, 53 (2004).
7. S. Tan and A. Haider, 2010 IEEE Int. Geosci. Remote. Sens. Symp. pp. 1178–1181 (2010).
8. S.-S. Lin, K. Yemelyanov, E. Pugh, and N. Engheta, IEEE Int. Conf. on Networking, Sens. Control. **1**, 216 (2004).
9. G. Anna, F. Goudail, and D. Dolfi, Opt. Express **19**, 25367 (2011).
10. I. J. Vaughn, B. G. Hoover, and J. S. Tyo, Proc. SPIE **8364**, 83640S1 (2012).
11. D. H. Goldstein, D. B. Chenault, and J. L. Pezzaniti, Proc. SPIE **3754**, 126 (1999).
12. D. H. Goldstein, Proc. SPIE **4133**, 112 (2000).
13. D. G. Jones, D. H. Goldstein, and J. C. Spaulding, Proc. SPIE **6240**, 62400A (2006).
14. C. G. Scarboro, C. J. Doherty, P. J. Balint-Kurti, and M. W. Kudenov, Appl. Opt. **61**, 9832 (2022).
15. A. De Martino, E. Garcia-Caurel, B. Laude, and B. Drévillon, Thin Solid Films **455**, 112 (2004).
16. K. Twietmeyer and R. Chipman, Opt. Express **16**, 11589 (2008).
17. D. Sabatke, M. Descour, E. Dereniak, *et al.*, Opt. Lett. **25**, 802 (2000).
18. J. S. Tyo, Appl. optics **41**, 619 (2002).
19. N. J. Field, M. R. Roddewig, and J. A. Shaw, Proc. SPIE **11833**, 175 (2021).
20. N. J. Field, "Simple monostatic mueller polarimeter control software," (2024).
21. N. J. Field, "Simple monostatic mueller polarimeter analysis software," (2024).

FULL REFERENCES

1. J. S. Tyo, D. L. Goldstein, D. B. Chenault, and J. A. Shaw, “Review of passive imaging polarimetry for remote sensing applications,” Appl. Opt. **45**, 5453–5469 (2006).
2. K. Sassen, “Polarization in lidar: a review,” Proc. SPIE **5158**, 151–160 (2003).
3. M. Floc’h, G. L. Brun, C. Kieleck, *et al.*, “Polarimetric considerations to optimize lidar detection of immersed targets,” Pure Appl. Opt. J. Eur. Opt. Soc. Part A **7**, 1327 (1998).
4. V. C. Vanderbilt, L. Grant, and C. S. Daughtry, “Polarization of light scattered by vegetation,” Proc. IEEE **73**, 1012–1024 (1985).
5. C. Rodríguez, E. Garcia-Caurel, T. Garnatje, *et al.*, “Polarimetric observables for the enhanced visualization of plant diseases,” Sci. reports **12**, 14743 (2022).
6. D. H. Goldstein and J. L. Cox, “Spectropolarimetric properties of vegetation,” Proc. SPIE **5432**, 53 – 62 (2004).
7. S. Tan and A. Haider, “A comparative study of polarimetric and non-polarimetric lidar in deciduous-coniferous tree classification,” 2010 IEEE Int. Geosci. Remote. Sens. Symp. pp. 1178–1181 (2010).
8. S.-S. Lin, K. Yemelyanov, E. Pugh, and N. Engheta, “Polarization enhanced visual surveillance techniques,” IEEE Int. Conf. on Networking, Sens. Control. **1**, 216–221 Vol.1 (2004).
9. G. Anna, F. Goudail, and D. Dolfi, “Optimal discrimination of multiple regions with an active polarimetric imager,” Opt. Express **19**, 25367–25378 (2011).
10. I. J. Vaughn, B. G. Hoover, and J. S. Tyo, “Classification using active polarimetry,” Proc. SPIE **8364**, 83640S1 (2012).
11. D. H. Goldstein, D. B. Chenault, and J. L. Pezzaniti, “Polarimetric characterization of spectralon,” Proc. SPIE **3754**, 126 – 136 (1999).
12. D. H. Goldstein, “Polarimetric characterization of federal standard paints,” Proc. SPIE **4133**, 112 – 123 (2000).
13. D. G. Jones, D. H. Goldstein, and J. C. Spaulding, “Reflective and polarimetric characteristics of urban materials,” Proc. SPIE **6240**, 62400A (2006).
14. C. G. Scarboro, C. J. Doherty, P. J. Balint-Kurti, and M. W. Kudenov, “Multistatic fiber-based system for measuring the mueller matrix bidirectional reflectance distribution function,” Appl. Opt. **61**, 9832–9842 (2022).
15. A. De Martino, E. Garcia-Caurel, B. Laude, and B. Drévillon, “General methods for optimized design and calibration of mueller polarimeters,” Thin Solid Films **455**, 112–119 (2004).
16. K. Twietmeyer and R. Chipman, “Optimization of mueller matrix polarimeters in the presence of error sources,” Opt. Express **16**, 11589–11603 (2008).
17. D. Sabatke, M. Descour, E. Dereniak, *et al.*, “Optimization of retardance for a complete stokes polarimeter,” Opt. Lett. **25**, 802–804 (2000).
18. J. S. Tyo, “Design of optimal polarimeters: maximization of signal-to-noise ratio and minimization of systematic error,” Appl. optics **41**, 619–630 (2002).
19. N. J. Field, M. R. Roddewig, and J. A. Shaw, “Near-monostatic angular mueller matrix measurements using a simple laser polarimeter,” Proc. SPIE **11833**, 175–185 (2021).
20. N. J. Field, “Simple monostatic mueller polarimeter control software,” (2024).
21. N. J. Field, “Simple monostatic mueller polarimeter analysis software,” (2024).